Plasma Flow Characteristics in a Spray-Type Dielectric Barrier Discharge Reactor

Hyun-Su Kim, Woo Seok Kang, Gon-Ho Kim, and Sang Hee Hong, *Member, IEEE*

***Abstract*—A numerical simulation on the spray-type dielectric barrier discharge (DBD) is carried out for a mixture gas of nitrogen (N_2) and sulfur hexafluoride (SF_6) at atmospheric pressure to understand the electrical characteristics and the plasma flow dynamics that depend on design parameters and operating conditions. A 2-D axi-symmetric nonuniform grid is employed in the simulation code consisting of the following three numerical modules: 1) discharge module; 2) flow module; and 3) reaction calculation module. Through the coupling of these modules, the discharge and plasma flow characteristics are interactively calculated for discharge properties and behaviors of charged and neutral particles in the N_2/SF_6 plasma, including 26 species interacting among them by 59 reactions. As a result of numerical simulations, the effects of the spray hole and the gas flow on the plasma flow characteristics are discussed in the spray-type DBD reactor. The existence of a spray hole in the grounded barrier/electrode plate induces strong electric fields along the spray hole barrier wall, and these high fields trigger a localized discharge similar to the surface discharge. The localized discharge spreads out in the discharge region toward the powered electrode barrier and gives the discharge current a pulsed shape according to the group behavior of a high-density electron to eventually produce a high-density fluorine atom in both the spray hole and spray regions. When the spray hole radius decreases, the fluctuations of hole-induced electric field also decreases, accompanied by the reduced production of average densities of the electron and the fluorine atom. However, the reduced spray hole size enhances the advective velocity along the hole axis, and therefore, the overall fluorine atom density over the substrate surface is increased. With increasing inlet gas flow velocity, the localized discharges occur more frequently because of electric potential formation by interacting among meta-stable species and ions to enhance the fluorine atom production. The fast advective velocity also enlarges the radial distributions of effluent rate and fluorine atom density in the spray region and on the substrate surface due to the transport of neutral particles.**

***Index Terms*—Atmospheric pressure nitrogen (N_2) and sulfur hexafluoride (SF_6) plasma, numerical simulation, plasma flow effect, spray-type dielectric barrier discharge (DBD).**

I. Introduction

DIELECTRIC barrier discharge (DBD), which is referred to as "silent discharge," is one of the most remarkable sources for generating nonequilibrium plasmas at atmospheric pressure [1]. Decisive advantages of the DBD include the ability to generate abundant reactive particles, such as atoms, radicals, ions, and excited species, by high-energy electron collisions with working gas particles operated even at the elevated pressure. Traditionally, the application of DBD to the industrial ozone synthesis has been commercialized for the past several tens of years. Nowadays, the use of DBD is extended to new application fields like environmental protection (pollution control, hazard waste destruction, etc.) [1]–[3], lighting and display industry (excimer lamps, plasma display panels, etc.) [1], and surface treatment (layer deposition modification, cleaning, etching, and ashing, etc.) [1], [4]. In the field of surface treatment in particular, the atmospheric DBD is a promising plasma source to replace low-pressure processing for etching or layer deposition since the DBD is operated at atmospheric pressure without using expensive vacuum facilities. Through this advantage of DBD in various industrial fields, numerous studies have suggested a variety of process reactors, such as atmospheric pressure plasma jet [5], hollow cathode discharge [6], coplanar barrier discharge [7], and one atmospheric uniform glow discharge plasma [8]. Recently, in thin-film transistor liquid-crystal display manufacturing, a spray-type DBD has been developed at the Korea Basic Science Institute, Seoul National University, and Samsung Electronics Company, Ltd., for the reduction of cost in large-area etching, ashing, and cleaning processes instead of the conventional low-pressure processes.

The spray-type DBD in a planar electrode arrangement has arrays of spray holes perforated on the grounded electrode surface covered with a dielectric barrier. The plasma-forming gas injected from both sides of the DBD reactor generates a plasma flow, including chemically reactive species, which is ejected through the spray holes into the spray region up to the substrate surface to create reactions among the species and the surface. Due to this configuration, the treatment area is the same as the electrode area to achieve an enlargement of treatment area easily. However, because of complex flow characteristics and nonuniform electric field generated by the hole structure, a numerical analysis of the spray-type DBD becomes very complicated. It is, therefore, required to investigate the discharge phenomena coupled with the flow effects for a better understanding of the plasma flow characteristics in the spray-type DBD reactor.

The aim of this work is to understand physical characteristics of the plasma flow dynamics influenced by various design and operating conditions for the spray-type DBD. A numerical code has been developed with a fully 2-D nonuniform grid of the spray-type reactor, and nitrogen (N_2) and an additive gas of sulfur hexafluoride (SF_6) are used as plasma-forming and

Manuscript received November 27, 2008; revised February 23, 2009 and March 9, 2009. First published April 28, 2009; current version published June 10, 2009. This work was supported in part by Samsung Electronics Company, Ltd., and in part by the Korea Science and Engineering Foundation.

The authors are with the Department of Nuclear Engineering, Seoul National University, Seoul 151-742, Korea (e-mail: khs0722@snu.ac.kr; stein@snu.ac.kr; ghkim@snu.ac.kr; hongsh@snu.ac.kr).

Color versions of one or more of the figures in this paper are available online at http://ieeexplore.ieee.org.

Digital Object Identifier 10.1109/TPS.2009.2018555

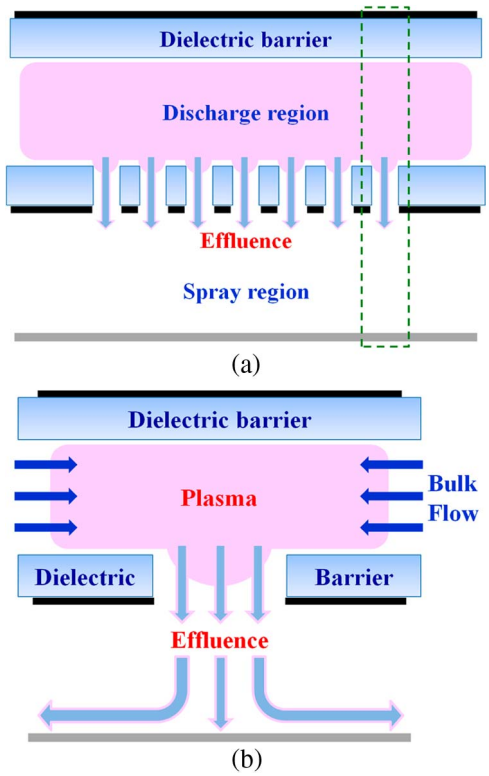

Fig. 1. Schematic diagrams of (a) a spray-type DBD reactor and (b) a computational region for a single hole in the spray-type DBD.

working gas, including 26 species related with 59 reactions. Using this simulation code, the plasma flow characteristics affecting neutral species behaviors are analyzed by focusing on the spray hole effect and the discharge dynamics. Moreover, changes of the discharge characteristics and the neutral species behaviors are examined with discharge current profiles and neutral species density distributions that vary with design parameters and operating conditions.

II. Numerical Simulation

The spray-type DBD reactor, which is actually used in an experiment for surface treatment, has the powered and grounded electrodes of 300 mm × 150 mm covered with 0.8-mm-thick alumina (Al_2O_3) plates that have a gap of 0.8 mm between them. The lower grounded electrode has thousands of 0.8-mm-radius holes that are perforated on it. A schematic diagram of the spray-type DBD is depicted in Fig. 1(a).

The computational domain of the spray-type DBD reactor considered in this numerical simulation is simplified to a single-hole region, as described in Fig. 1(b). The 2-D axi-symmetric cylindrical coordinates are applied to the numerical simulation code based on a nonuniform staggered grid system shown in Fig. 2, indicating important positions and regions. The spray-type DBD simulation code consists of the following three coupled numerical modules: 1) discharge simulation; 2) flow simulation; and 3) reaction calculation. In the discharge module, charged species properties and electric field distributions are calculated, while flow velocity fields and neutral species behaviors are computed in the flow module. The reaction module calculates the source and sink terms of charged and neutral

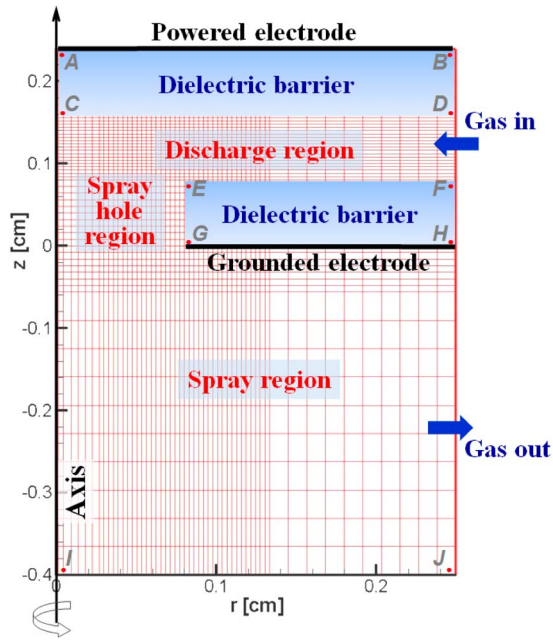

Fig. 2. Computational domain of a 2-D axi-symmetric simulation model for the spray-type DBD reactor.

species resulted from physical and chemical reactions among plasma species generated through the DBD. The discharge and flow modules are linked with outputs of the reaction calculation, and a time slicing method is taken into account for two different time scales of discharge interaction and plasma flow. Considering the linkage between the flow and discharge modules, the time scale of the flow module should be determined as close as possible to that of the discharge module. Since the distributions of space charges are sensitively changed by the reactions between charged and neutral particles, a minute change in the neutral particle distribution can make significant effects on the discharge characteristics. The typical values of time scales are 10 ps in the discharge and reaction modules ($\Delta t_{\text{discharge}} = \Delta t_{\text{reaction}} = 10$ ps) and 10 ns in the flow module ($\Delta t_{\text{flow}} = 10$ ns). The flow module is then calculated every 1000 time step of discharge and reaction calculations. The computing time executed on a Pentium-4 personal computer (2.8-GHz central processing unit, 1-GB random access memory, and LINUX operating system) is about 10 h for 10-μs time marching in the simulation.

A. Discharge Simulation Module

1) Governing Equations: A fluid model based on magnetohydrodynamic theory is employed for the present numerical simulation, which is involved in the interaction of charged particles in the electric field $\mathbf{E}$. The motions of electrons, positive ions, and negative ion species are described by their continuity equations, which are described as follows:

$$\frac{\partial n_k}{\partial t} + \nabla \cdot (n_k \mathbf{v}_k) = S_k \tag{1}$$

$$\mathbf{v}_k = \mu_k \mathbf{E} \tag{2}$$

where n_k, $\mathbf{v}_k$, S_k, and μ_k are the number density, drift velocity, source and sink terms, and mobility, respectively, and

TABLE I
MOBILITY OF POSITIVE AND NEGATIVE ION SPECIES GENERATED BY DBD IN THE N_2/SF_6 MIXTURE PLASMA

Ion species	Mobility [$cm^2/V{\cdot}s$]			Ref.
	E/N<120 Td	120<E/N <350 Td	350 < EN	
N_2^+	3.714			[22]
N_4^+	1.857			-
SF_6^+	0.6	0.1216 ln(E/N)	1.827 -0.1897 ln(E/N)	[23]
SF^+	1.7162	0.3478 ln(E/N)	5.226 -0.5426 ln(E/N)	-
S^+	2.7329	0.5539 ln(E/N)	8.322 -0.8641 ln(E/N)	-
F_2^+	2.3063	0.4674 ln(E/N)	7.023 -0.7292 ln(E/N)	
SF_6^-	$1.690\times10^{-10}(E/N)^2$			[23]
SF_5^-	$1.943\times10^{-10}(E/N)^2$			-
SF_4^-	$2.284\times10^{-10}(E/N)^2$			-
SF_3^-	$2.772\times10^{-10}(E/N)^2$			-
SF_2^-	$3.523\times10^{-10}(E/N)^2$			-
F_2^-	$6.496\times10^{-10}(E/N)^2$			-
F^-	$1.299\times10^{-09}(E/N)^2$			-

the subscript k denotes the identity of electron, positive ion, and negative ion. The drift motions of charged species are decided mainly by their mobility since their diffusion motions are relatively negligible in a strong electric field of discharge.

The mobility of electron is determined by a local electric field $\mathbf{E}$ from local field approximations. It is assumed that plasma properties, such as electron drift velocity and collisional ionization coefficient, are functions of reduced electric field E/N, where E is the electric field magnitude, and N is the particle number density. Essentially, this means that the electron energy distribution function (EEDF) is in local equilibrium with neutral plasma [9]. The EEDF $f(\varepsilon)$ is calculated from the following spatially homogeneous Boltzmann equation [10]:

$$\frac{\partial f}{\partial t} + \frac{e\mathbf{E}}{m} \cdot \nabla_v f = \left.\frac{\partial f}{\partial t}\right|_{\text{collisions.}} \tag{3}$$

The electron mobility μ_e is then obtained from EEDF using the following integral [10]:

$$\mu_e = \frac{1}{3}\sqrt{\frac{2}{m_e}} \int \frac{\varepsilon}{N\sigma(\varepsilon)} \frac{\partial f(\varepsilon)}{\partial \varepsilon} d\varepsilon \tag{4}$$

where ε and m_e are the energy and mass of electron, respectively. The mobilities of positive and negative ion species listed in Table I are calculated from the following equation and from the data of reference species:

$$\mu_i = \frac{e}{m_i \nu_m} \tag{5}$$

where m_i is the mass of ion species, and ν_m is the collision frequency for momentum transfer, which is a function of gas temperature at a constant pressure [11].

The electric potential ϕ, which is to be used for the calculation of the electric field, is determined by Poisson's equation, i.e.,

$$\nabla \cdot (\varepsilon_r \nabla \phi) = -\frac{e}{\varepsilon_0}(n_p - n_n - n_e) \tag{6}$$

$$\mathbf{E} = -\nabla \phi \tag{7}$$

where ε_0 is the dielectric constant of free space, ε_r is the relative permittivity, and e is the electron charge.

The discharge current I in the discharge region is calculated from Sato's equation, with a time-dependent applied voltage [12], i.e.,

$$I = \frac{e}{V_a}\int_V (n_p\mathbf{v}_p - n_n\mathbf{v}_n - n_e\mathbf{v}_e)\cdot\mathbf{E}_L dv + \frac{\varepsilon_0}{V_a}\int_V \frac{\partial \mathbf{E}_L}{\partial t}\cdot\mathbf{E}_L dv \tag{8}$$

where V_a is the externally applied voltage, and $\mathbf{E}_L$ is the space charge free component of electric field. In (8), the first term in the right-hand side is the conduction current, and the second term is the displacement current.

2) Boundary Conditions: The boundary conditions for charged species density are given by the Neumann conditions, as listed in Table II(a). The boundary values of the electric potential at the powered and grounded electrodes are given by the Dirichlet conditions, while those at the substrate surface, i.e., flow inlet and outlet, are expressed by the Neumann conditions, as summarized in Table II(a).

At the plasma–dielectric barrier boundaries, Gauss's and Stokes's theorems are applied to Gauss's and Faraday's laws, respectively, to get the boundary conditions for the electric potential that resulted to [13]

$$\varepsilon_p \nabla\phi_p \cdot \mathbf{n} - \varepsilon_d \nabla\phi_d \cdot \mathbf{n} = e(\sigma_{\text{positive}} - \sigma_{\text{negative}}) \tag{9}$$

$$\mathbf{n} \times (\nabla\phi_p - \nabla\phi_d) = 0 \tag{10}$$

where ε, σ, and $\mathbf{n}$ are the permittivity of the material, the surface charge density, and the unit normal vector from plasma

TABLE II
BOUNDARY CONDITIONS FOR (a) DISCHARGE AND (b) FLOW CALCULATIONS

(a)

Boundary	Location in Fig. 2	Electric potential	Charged particle density
Powered electrode	A-B	$\phi = V_{external}$	-
Grounded electrode	G-H	$\phi = 0$	$\nabla n_i = 0$
Plasma-barrier boundary	C-D, E-F E-G	$\varepsilon_p \nabla\phi_p \cdot \mathbf{n} - \varepsilon_d \nabla\phi_d \cdot \mathbf{n} = e(\sigma_{positive} - \sigma_{negative})$ $\mathbf{n} \times (\nabla\phi_p - \nabla\phi_d) = 0$	$\nabla\Gamma_i = 0$
Flow inlet Flow outlet	D-F H-J	$\nabla\phi = 0$	$\nabla n_i = 0$
Substrate surface	I-J	$\nabla\phi = 0$	$\nabla n_i = 0$

(b)

Boundary	Location in Fig. 2	Neutral particle density	Velocity	Pressure correction term
Flow inlet	D-F	$\nabla n_i = 0$	$\mathbf{V}$ = constant	$\nabla p' = 0$
Flow outlet	H-J	$\nabla n_i = 0$	$\nabla \mathbf{V} = 0$	$\nabla p' = 0$
Barrier walls Substrate surface	C-D, E-F E-G I-J	$\nabla n_i = 0$	$\mathbf{V} = 0$	$\nabla p' = 0$

toward the dielectric barrier, respectively. The subscripts p and d indicate plasma and dielectric barrier, respectively. At the dielectric barrier surfaces, all of the charge fluxes moving toward the dielectric barriers are assumed to be accumulated on the dielectric surfaces without dissipation or loss. Equations of positive and negative surface charge densities (i.e., σ_p and σ_n) are given by

$$\frac{\partial \sigma_p}{\partial t} = n_p \mathbf{v}_p \cdot \mathbf{n} \tag{11}$$

$$\frac{\partial \sigma_n}{\partial t} = n_n \mathbf{v}_n \cdot \mathbf{n} + n_e \mathbf{v}_e \cdot \mathbf{n}. \tag{12}$$

3) Numerical Scheme: The continuity equations for charged species are solved using an explicit upwind scheme in a structured nonuniform grid system. The modified grids, which are refined according to the reactor geometry, reduce the artificial diffusion in the upwind scheme [14]. The sizes of the grids are determined by the Courant–Friedrichs–Lewy condition for the minimum artificial diffusion and the stability of simulation [15]. In the calculation of the electric potential, Poisson's equation is explicitly solved using the finite-difference method (FDM) in the same grid system with calculation of the continuity equations. The discretized Poisson's equation is converted to a matrix form, and it is calculated by a fast direct method using a sparse matrix solver, namely, the UMFPACK library [16]. The electric field is computed using linear interpolation of derivative of the electric potential.

B. Flow Simulation Module

In this simulation, the gas flow is assumed to consist of the following two components: 1) a steady-state bulk flow and 2) an advected stream of neutral particles [17]. The steady-state bulk flow is computed for the average advective velocity of plasma flow, which determines the velocities of neutral species all the time. These velocities advect the number densities of neutral species, whose sink or source terms are updated in the reaction calculation module. The calculation procedure in the flow module is also repeated for time marching, but its time scale ($\Delta t_{\text{flow}} = 10$ ns) is 10^3 times longer than the time scale of discharge ($\Delta t_{\text{discharge}} = 10$ ps) due to the bulk phenomena in the flow.

TABLE III
CHARGED AND NEUTRAL SPECIES PRODUCED BY DBD IN THE N_2/SF_6 MIXTURE PLASMA

	N_2 related species	SF_6 related species
Charged particles	N_2^+, N_4^+, e	SF_6^+, SF^+, S^+, F_2^+, SF_6^-, SF_5^-, SF_4^-, SF_3^-, SF_2^-, F_2^-, F^-, e
Atoms	-	S, F
Molecules	N_2	SF_6, SF_5, SF_4, SF_3, SF_2, SF, F_2
Excited species	$N_2(A^3\Sigma_u^+)$, $N_2(a'^1\Sigma_u^-)$, $N_2(B^3\Pi_g)$, $N_2(C^3\Pi_u)$	SF_6(v), SF_6(e1), F_2(v), F_2(e1), F(m1), F(e2)

1) Governing Equations: The typical plasma flow velocity in the spray-type DBD is in the range of ~10 m/s, which is treated as incompressible flow [14]. The reactor is assumed to be operated with a constant inlet flow rate of steady-state bulk flow. The Newtonian fluid with constant viscosity is applied for linearization of diffusion terms. As a result, the bulk velocity field is expressed in tensor notations by mass

TABLE IV
PHYSICAL AND CHEMICAL REACTIONS WITH N_2 SPECIES AND THEIR CORRESPONDING RATE COEFFICIENTS IN DBD

	Reactions	k	Ref.
(1)	$N_2 + e \rightarrow N_2(A^3\Sigma_u^+) + e$	f(E/N)	[18]
(2)	$N_2 + e \rightarrow N_2(a'^1\Sigma_u^-) + e$	f(E/N)	[18]
(3)	$N_2 + e \rightarrow N_2(B^3\Pi_g) + e$	f(E/N)	[18]
(4)	$N_2 + e \rightarrow N_2(C^3\Pi_u) + e$	f(E/N)	[18]
(5)	$N_2 + e \rightarrow N_2^+ + e + e$	f(E/N)	[18]
(6)	$N_4^+ + e \rightarrow N_2 + N_2$	$1.1\times10^{-7}\times Te^{-0.5}$ cm^3s^{-1}	[24]
(7)	$N_2^+ + e \rightarrow 2N$	$1.6\times10^{-8}\times Te^{-0.5}$ cm^3s^{-1}	[25]
(8)	$N_2^+ + e \rightarrow N_2(D) + N$	$1.1\times10^{-8}\times Te^{-0.5}$ cm^3s^{-1}	[25]
(9)	$N_2(A^3\Sigma_u^+) + N_2(a'^1\Sigma_u^-) \rightarrow N_4^+ + e$	5.0×10^{-11} cm^3s^{-1}	[24]
(10)	$N_2(a'1\Sigma u-) + N_2(a'^1\Sigma_u^-) \rightarrow N_4^+ + e$	2.0×10^{-10} cm^3s^{-1}	[24]
(11)	$N_2(A^3\Sigma_u^+) + N_2(A^3\Sigma_u^+) \rightarrow N_2(B^3\Pi_g) + N_2(X^1\Sigma_g^+)$	7.7×10^{-11} cm^3s^{-1}	[24]
(12)	$N_2(A^3\Sigma_u^+) + N_2(A^3\Sigma_u^+) \rightarrow N_2(C^3\Pi_u) + N_2(X^1\Sigma_g^+)$	3.0×10^{-12} cm^3s^{-1}	[24]
(13)	$N_2(A^3\Sigma_u^+) + N_2 \rightarrow N_2(X^1\Sigma_g^+) + N_2$	3.0×10^{-18} cm^3s^{-1}	[24]
(14)	$N_2(a'^1\Sigma_u^-) + N_2 \rightarrow N_2(B^3\Pi_g) + N_2$	2.0×10^{-13} cm^3s^{-1}	[24]
(15)	$N_2(B^3\Pi_g) + N_2 \rightarrow N_2(A^3\Sigma_u^+) + N_2$	5.0×10^{-11} cm^3s^{-1}	[24]
(16)	$N_2(C^3\Pi_u) + N_2 \rightarrow N_2(a'^1\Sigma_u^-) + N_2$	1.0×10^{-11} cm^3s^{-1}	[24]
(17)	$N_2^+ + N_2(A^3\Sigma_u^+) \rightarrow N_3^+ + N_2$	3.0×10^{-10} s^{-1}	[24]
(18)	$N_4^+ + N_2 \rightarrow N_2 + 2N_2$	2.4×10^{-15} cm^3s^{-1}	[24]
(19)	$N_2(a'^1\Sigma_u^-) + N_2 \rightarrow N_2(X^1\Sigma_g^+) + N_2(X^1\Sigma_g^+)$	2.0×10^{-13} cm^3s^{-1}	[24]
(20)	$N_2(B^3\Pi_g) \rightarrow N_2(A^3\Sigma_u^+) + h\nu$	1.5×10^{5} s^{-1}	[25]
(21)	$N_2(C^3\Pi_u) \rightarrow N_2(B^3\Pi_g) + h\nu$	3.0×10^{7} s^{-1}	[25]

conservation and Navier–Stokes equations, respectively, as follows:

$$\frac{\partial}{\partial x_j}(\rho v_j) = 0 \tag{13}$$

$$\frac{\partial}{\partial x_j}(\rho v_i v_j) = \frac{\partial}{\partial x_j}\left(\mu \frac{\partial v_i}{\partial x_j}\right) - \frac{\partial p}{\partial x_i} \tag{14}$$

where ρ, μ, and p are the mass density, viscosity, and pressure of plasma fluid, respectively. The motions of neutral species are also described by the following continuity equation:

$$\frac{\partial n_i}{\partial t} + \nabla \cdot (n_i \mathbf{v}_i) = S_i \tag{15}$$

where the subscript i designates the neutral species of atoms, molecules, radicals, and excited species, respectively.

2) Boundary Conditions: As the boundary conditions of bulk velocity field, a steady flow condition is employed for the flow inlet boundary (D–F), and the Neumann condition is used at the flow outlet boundary (H–J). At all of the solid walls, including the dielectric barrier surfaces (C–D, E–F, and E–G), grounded electrode surface (G–H), and substrate plate (I–J), the nonslip condition is applicable because of wall effect. The pressure correction terms p' at the entire boundaries are obtained from the Neumann condition.

The boundary values of neutral species density are calculated from the Neumann condition at all the boundaries of the computation region, including the substrate plate (I–J). Surface reactions over the substrate surface (I–J) are not included in this simulation. Although the reactions of meta-stables with the substrate are important phenomena, the mechanisms of the surface reactions are not yet sufficiently understood in a high-pressure nonequilibrium plasma condition. However, the relevant surface reaction effects by plasma, such as etching, ashing, and cleaning, are expected from the flux distributions of meta-stables over the substrate, which should be considered in a future extended work.

The boundary conditions for the flow simulation are summarized in Table II(b).

3) Numerical Scheme: The mass conservation equation in (13) and Navier–Stokes equations (14) for the steady-state flow are discretized using a finite-volume nonuniform staggered grid system. The discretized equations are calculated using a

TABLE V
PHYSICAL AND CHEMICAL REACTIONS WITH SULFUR FLUORIDE SPECIES AND THEIR CORRESPONDING RATE COEFFICIENTS IN DBD

	Reactions	k	Ref.		Reactions	k	Ref.
(1)	$SF_6 + e \leftrightarrow SF_6(v) + e$	f(E/N)	[19, 26]	(20)	$F(m1) + e \rightarrow F^+ + 2e$	f(E/N)	[19, 27]
(2)	$SF_6 + e \leftrightarrow SF_6(e1) + e$	f(E/N)	[19, 26]	(21)	$S + e \rightarrow S(e1) + e$	f(E/N)	[19, 28]
(3)	$SF_6 + e \rightarrow SF_6^-$	f(E/N)	[19, 26]	(22)	$S + e \rightarrow S(e2) + e$	f(E/N)	[19, 28]
(4)	$SF_6 + e \rightarrow SF_6^+ + 2e$	f(E/N)	[19, 26]	(23)	$S + e \rightarrow S^+ + 2e$	f(E/N)	[19, 28]
(5)	$SF_6 + e \rightarrow SF_5^- + F$	f(E/N)	[19, 26]	(24)	$SF_6 + e \rightarrow SF_4 + F_2 + e$	a)	[29]
(6)	$SF_6 + e \rightarrow F^- + SF_5$	f(E/N)	[19, 26]	(25)	$SF_4 + e \rightarrow SF_2 + F_2 + e$	b)	[29]
(7)	$SF_6 + e \rightarrow SF_4^- + F_2$	f(E/N)	[19, 30]	(26)	$SF_2 + e \rightarrow S + F_2 + e$	c)	[29]
(8)	$SF_6 + e \rightarrow SF_4^- + 2F$	f(E/N)	[19, 30]	(27)	$SF_2 + e \rightarrow SF + F + e$	d)	[29]
(9)	$SF_6 + e \rightarrow SF_3^- + F_2 + F$	f(E/N)	[19, 30]	(28)	$SF + e \rightarrow SF^+ + 2e$	e)	[29]
(10)	$SF_6 + e \rightarrow SF_2^- + 2F_2$	f(E/N)	[19, 30]	(29)	$F_2(v) + e \rightarrow 2F + e$	f)	[29]
(11)	$SF_6 + e \rightarrow F_2^- + SF_4$	f(E/N)	[19, 30]	(30)	$SF^+ + e \rightarrow S + F$	3.16×10^{-07}	[29]
(12)	$F_2 + e \rightarrow F^- + F$	f(E/N)	[19, 31]	(31)	$S^+ + F_2 \rightarrow SF^+ + F$	5.89×10^{-10}	[29]
(13)	$F_2 + e \rightarrow F_2^+ + 2e$	f(E/N)	[19, 32]	(32)	$SF_6^- + SF_6^+ \rightarrow 2SF_6$	1.00×10^{-08}	[29]
(14)	$F_2 + e \rightarrow F_2(e1) + e$	f(E/N)	[19, 32]	(33)	$SF_4 + F \rightarrow SF_3 + F_2$	2.32×10^{-15}	[33]
(15)	$F_2 + e \rightarrow 2F + e$	f(E/N)	[19, 34]	(34)	$SF_2 + F \rightarrow SF_3$	4.11×10^{-19}	[33]
(16)	$F_2 + e \rightarrow F_2(v) + e$	f(E/N)	[19, 35]	(35)	$SF + F_2 \rightarrow SF_3$	3.61×10^{-19}	[33]
(17)	$SF + e \rightarrow F^- + S$	f(E/N)	[19, 31]	(36)	$SF_3 + F \rightarrow SF_4$	8.53×10^{-11}	[33]
(18)	$F + e \rightarrow F(e2) + e$	f(E/N)	[19, 36]	(37)	$SF_3 + SF_3 \rightarrow SF_2 + SF_4$	7.89×10^{-11}	[33]
(19)	$F + e \rightarrow F(m1) + e$	f(E/N)	[19, 36]	(38)	$SF_3 + F_2 \rightarrow SF_5$	4.16×10^{-19}	[33]

a) $3.0\times10^{-08}\times\exp(-6.22/T_e)$ b) $3.0\times10^{-08}\times\exp(-6.22/T_e)$ c) $3.0\times10^{-08}\times\exp(-6.22/T_e)$
d) $3.0\times10^{-08}\times\exp(-3.00/T_e)$ e) $3.0\times10^{-14}\times\exp(-10.79/T_e)$ f) $3.0\times10^{-08}\times\exp(-0.69/T_e)$

semi-implicit method for pressure-linked equations algorithm [18]. This algorithm is one of the implicit pressure-correction techniques, i.e., once the pressure correction equation has been solved, the velocities are updated using the pressure correction term. Since the pressure is defined at the center of the grid cell, the boundary values of pressure can be calculated from boundary velocities that are defined by cell surface [14]. The continuity equation in (15) for neutral species is discretized on the basis of the FDM and is solved using an explicit upwind scheme in the same way as the charged particle continuity equations in (1) and (2).

C. Reaction Calculation Module

In this module, the source or sink terms of charged and neutral species are calculated and updated for each particle density at each time step in the discharge and flow simulation modules. The source and sink terms of charged and neutral species in (1) and (15) are found by particle collision reactions in the DBD plasma. According to the local field approximation, the rate constants of electron collision reactions are expressed as functions of the reduced electric field $f(E/N)$. The field-dependent rate coefficients are computed from the following EEDF integrals [10]:

$$k_k = \int \sigma_k(\varepsilon) f(\varepsilon) d\varepsilon \tag{16}$$

where k_k and σ_k are the rate constant and the cross section of k reaction, respectively. The EEDF for calculation of rate constants is found from a numerical Boltzmann solver, called BOLSIG [19]. The source and sink terms S_i of each species are calculated from the following rate equation:

$$\frac{\partial S_i}{\partial t} = \sum_k k_k [A][B] \tag{17}$$

where A and B are the reactant concentrations of k reaction related with i species.

In the present numerical simulation, N_2 is used as a plasma-forming gas and SF_6 as a reaction gas. Seven species of N_2 and 26 species of sulfur fluoride, as listed in Table III, are involved in the physical and chemical reactions by DBD in the N_2/SF_6 mixture plasma, and their corresponding rate constants for N_2 and SF_6 are presented in Tables IV and V.

In general, the gas heating effect is significantly stressed in some cases of atmospheric-pressure nonequilibrium plasmas that show high gas temperatures of even over 1000 K. However, authors' experimental results with a spray-type DBD showed below 400 K of the gas temperature in this spray-type reactor. Although the temperature-dependent reactions are adopted in this simulation, such as reactions (33)–(38) in Table V, the variations of the reaction coefficients are small in the temperature range 300–400 K. For this reason, the temperature-dependent effect on the rate constants is negligible, and the gas temperature is assumed to be constant at 300 K, and the effect of gas heating is not considered in this simulation.

TABLE VI
DESIGN PARAMETERS AND OPERATING CONDITIONS FOR THE SIMULATION

Design parameters				Operating conditions					
Discharge gap	Barrier material	Barrier thickness	Spray-hole radius	Applied voltage	Operating frequency	Plasma / additive gas	Inlet flow velocity	Gas temperature	Operating pressure
0.8 mm	Al_2O_3	0.8 mm	0.4, 0.8[a] mm	6.5 kV	20 kHz	N_2 97 % / SF_6 3%	4, 8[a] m/s	300 K	700 torr[b]

[a] The base conditions of simulation.

[b] Operating pressure is set from the experimental condition which is slightly lower than 1 atm for a safe ventilation of the hazardous gas.

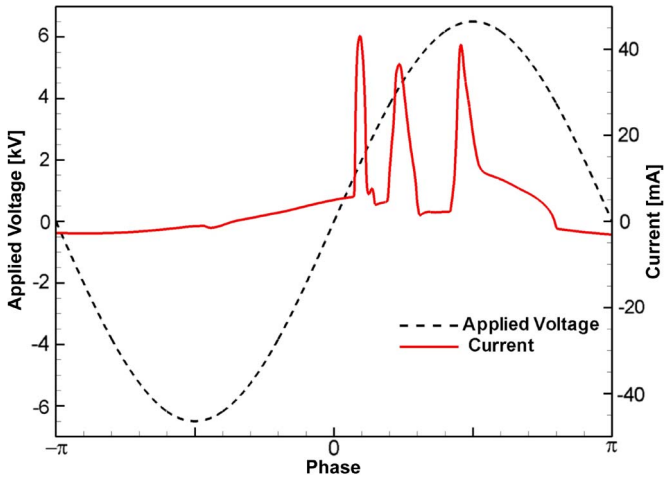

Fig. 3. Applied voltage and discharge current profiles in the spray-type DBD.

III. SIMULATION RESULTS

A. Plasma Flow Characteristics

The design parameters and operating conditions are determined by experimental research, which has been performed in the authors' laboratory, and the simulation parameters, including the base conditions, are summarized in Table VI.

In the base simulation, the discharge and plasma flow characteristics are examined by focusing on the effect of the spray hole and the behavior of the fluorine atom as a reacting species. The spray-type DBD has the multipulsed current characteristic that appears in Fig. 3, obtained from the base simulation. This pulsed current behavior is attributed to the group behavior of the high-density electrons, which starts from the spray hole barrier wall (E–G). The detailed progress of electron and electric field movements corresponding to the discharge phase is found from a series of numerical images in Fig. 4. In the first phase, a strong electric field is induced at the exit of the spray hole barrier wall and triggers a rapid production of electrons. A localized discharge is then formed over the spray hole barrier wall similar to a surface discharge [20]. In the second phase, the surface discharge grows along with the spread of the high-electron-density region to the discharge region. In addition, the electric field at the spray hole barrier wall is reduced due to a decrease in the potential difference between the surface discharge region and the barrier wall on which negative charges are accumulated. After the peak of pulsed current, the high-electron-density region moves toward the powered electrode barrier surface and becomes extinct at the same time in the discharge region. The electric field is maintained relatively low until the electric potential rises sufficiently high in the spray hole. This phenomenon is repeated during the half period of the positive applied voltage, and these peaked pulses are similar to a typical current shape of the filamentary DBD [21], but their durations are much longer than those of the filamentary DBD. In contrast to the positive period of the applied voltage, its negative period has no peaks in the current profile. The group behavior of the electrons from the powered electrode barrier surface to the grounded electrode barrier exists during the half period of the negative applied voltage, but the produced electron density is too low to affect the discharge current. Since the powered electrode barrier surface has no spray hole contrary to the grounded electrode, high intensities of electric field cannot be induced to generate a sufficient electron density affecting the discharge current profile.

The average advection velocity distribution in the spray-type DBD reactor is drawn along with its stream lines in Fig. 5. The N_2/SF_6 mixture gas enters with 8 m/s through the outer boundary of discharge region (D–F). The accelerated flow ejected to the substrate makes a back flow going around the spay hole barrier wall (E–G) and has the maximum velocity at the center of the spray region. Then, the ejected flow from the spray hole reaches the substrate surface and spreads out to the flow outlet along the substrate surface. Fig. 6 shows the temporal density distributions of fluorine atoms at 30, 50, and 70 μs. Fluorine atoms produced in the discharge and spray hole regions are ejected through the spray hole to the substrate. The fluorine atoms near the spray hole barrier wall (E–G) are produced more than those in other regions, because abundant electrons are produced by the surface discharge over the spray hole barrier wall to enhance fluorine atom production. Consequently, it is concluded that the surface discharge in the spray hole geometry can affect the density distributions of neutral species like the fluorine atom in the spray region.

B. Effects of Spray Hole Radius

For a better understanding of spray hole effects, the spray hole radius is reduced to 0.4 mm, which is half of that of the base simulation condition, and the other conditions are unchanged in this comparative simulation.

The current profile for 0.4 mm radius is shown in Fig. 7(a), as compared with that of the base condition. The electric field distributions at the initial moment of the first current pulse are shown in Fig. 7(b), and the electron density distributions at the peak moment of the first current pulse are seen in Fig. 7(c).

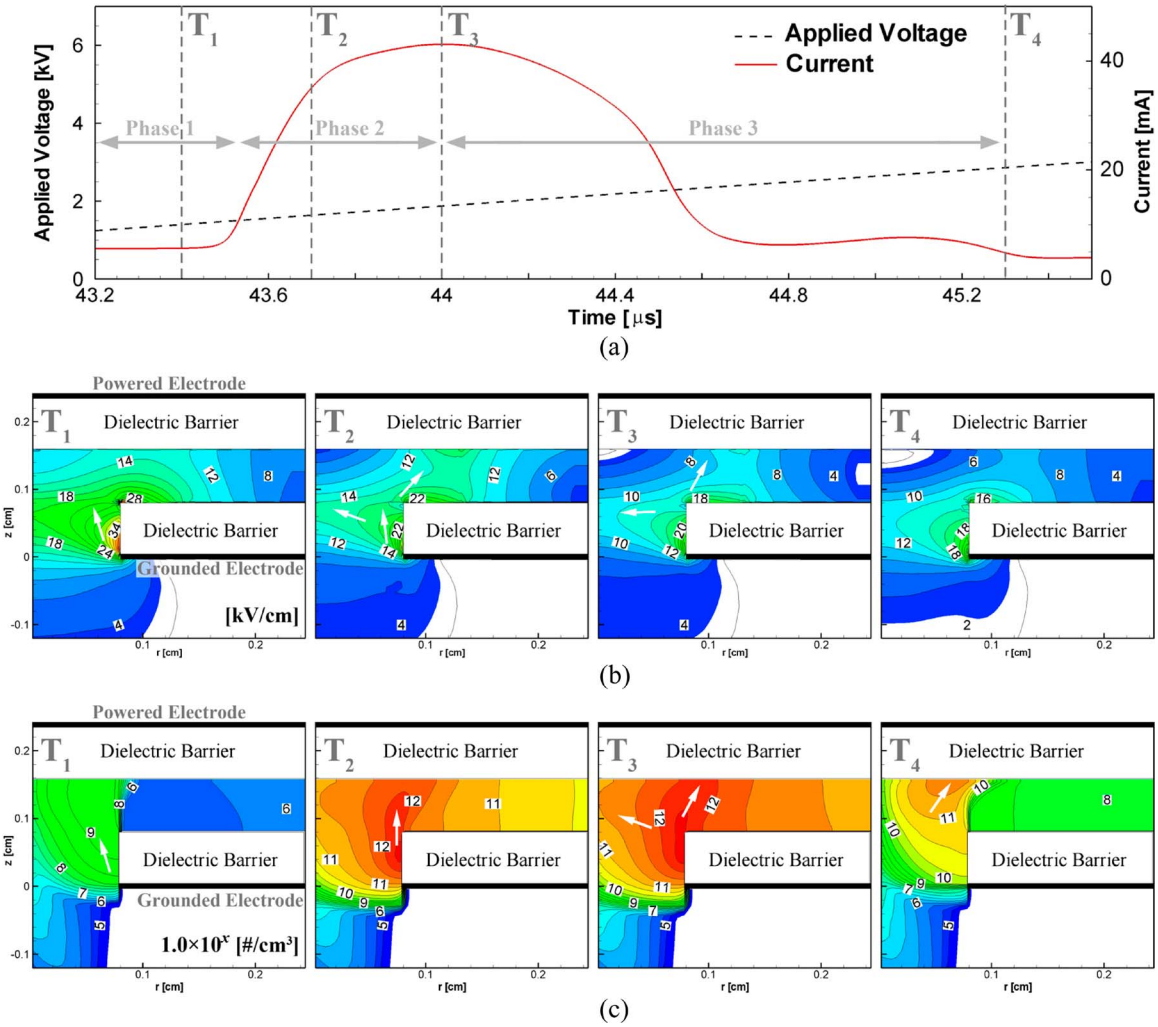

Fig. 4. (a) Enlarged shape of peaked current profile and spatial distributions of (b) electric field and (c) electron density according to the discharge phase in the spray-type DBD reactor. [T_1, T_2, T_3, and T_4 represent the discharge moments appeared in (a), respectively, and the number at each contour in (b) indicates the order x of electron density in 10^x cm^{-3} unit.]

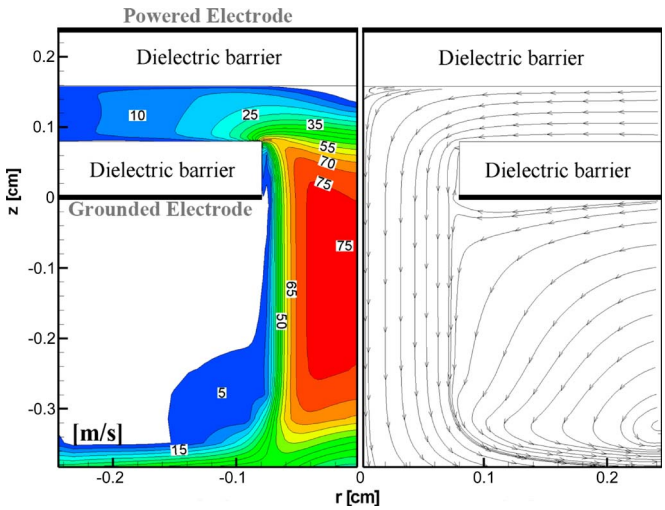

Fig. 5. (Left) Average advection velocity distribution and (right) its flow stream lines in the spray-type DBD reactor.

As the spray hole radius decreases, the intensity and number of peaked current are reduced with longer peak intervals. This result means that the localized discharge formed at the spray hole barrier wall (E–G) of 0.4 mm in radius has a lower electron density and longer potential recovery time to reach a sufficiently high electric field. The maximum electric field for a 0.4-mm radius appears at the spray hole barrier surface to be 35 kV/cm, which is relatively lower than that in excess of 40 kV/cm for the base simulation. As the level of the localized discharge triggered by the electric field is low, the high-electron-density region is shrunk, and the electron density in the whole discharge region decreases. The smaller hole radius reduces the activity of the discharge dynamics in the reactor.

C. Effects of Inlet Flow Velocity

In Fig. 8, for the average advection velocity, the reduced spray hole radius produces a much faster velocity flow in the spray hole. This faster advection velocity enhances the transport of neutral species particles resulted in a high effluent rate of fluorine atoms. Fig. 9, showing the fluorine density distributions for both hole radii, indicates that the higher effluent rate at the spray hole exit results in a higher density of the fluorine atom, which has the advantage of processing rate enhancement.

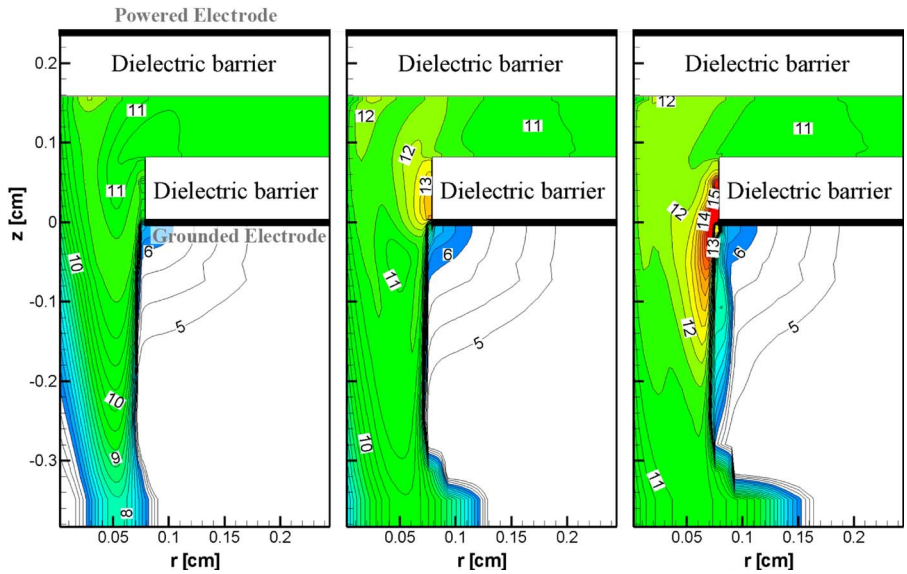

Fig. 6. Temporal density distributions of fluorine atoms at 30, 50, and 70 μs in the spray-type DBD reactor. (The number at each contour indicates the order x of density in 10^x cm^{-3} unit.)

In the aspect of the spatial distribution, however, the large spatial differences in velocity for a 0.4-mm hole radius cause a nonuniform density distribution of fluorine atoms on the substrate surface. This spatial nonuniformity is disadvantageous to the large-area surface processing. Consequently, the spray hole radius has the tradeoff effect on the effluence rate and the distribution of neutral species.

The effects of advective flow velocity are found by reducing the inlet flow velocity to 4 m/s, which is half of that of the base simulation, and the other conditions are kept the same. The current profiles shown in Fig. 10 reveal that the number of pulsed current peaks decreases with longer peak intervals as the inlet flow velocity decreases. This result indicates that the flow of gas can affect the spray-type DBD characteristics through bulk movements of neutral species that interact with heavily charged species of positive and negative ions.

In the present N_2/SF_6 mixture DBD, the N_4^+ ion is mainly produced by associative ionizations of the two meta-stables among reactions in Table IV. We have

$$N_2\left(A^3\Sigma_u^+\right) + N_2\left(a'^1\Sigma_u^-\right) \rightarrow N_4^+ + e$$
$$N_2(a'1\Sigma u-) + N_2\left(a'^1\Sigma_u^-\right) \rightarrow N_4^+ + e.$$

The N_4^+ ion species plays an important role in the formation of a space charge source in Poisson's equation for the electric potential calculation. That is, the meta-stables formed by the advection of flow affect the distribution of the N_4^+ ion species that have an effect on the electric potential formation. Therefore, the flow effects cause the electrical characteristics to change through interactions among $N_2(a'^1\Sigma_u^-)$, $N_2(A^3\Sigma_u^+)$, and N_4^+ ion.

Fig. 11(a) and (b) plots the radial density distributions of $N_2(a'^1\Sigma_u^-)$ and N_4^+, respectively, on the spray hole exit surface $(z = 0)$, depending on the inlet flow velocity. The $N_2(a'^1\Sigma_u^-)$ meta-stable density increases with increasing inlet flow velocity due to its fast transport from the localized discharge region to the spray hole exit. The low density of the meta-stable leads the N_4^+ ion species to reduce its production rate. The reduced production rate of N_4^+ takes longer to accumulate space charges that are related to the electric potential at the spray hole exit (G). The fluorine density distributions, which depend on the inlet flow velocity, are shown in Fig. 12. As the inlet flow velocity increases, the high-density regions of the fluorine atoms are reduced in the discharge and spray hole regions, while they are widened in the spray region. This phenomenon means that the transport of neutral particle moving through the discharge to spray regions is gradually developed along the radial direction as the increment of average advective velocity. Therefore, the high advective flow velocity has the advantage of enhancing the process rate on the substrate.

IV. Conclusion

A numerical simulation of atmospheric pressure DBD in a spray-type reactor for surface treatment has been accomplished to understand the characteristics of plasma flow influenced by the reactor design and operation parameters, such as spray hole radius and inlet gas flow.

A numerical simulation code for the N_2/SF_6 DBD plasma with a flow ejection from the spray hole in the grounded electrode has been developed with a fully 2-D (r, z) nonuniform grid in axi-symmetric $(\partial/\partial\theta = 0)$ coordinates. This numerical code consists of three modules for discharge, flow, and reaction calculation. Spatial and temporal distributions of electric field and charged species densities are calculated in the discharge module, and advective velocity fields and neutral species characteristics are computed in the flow module, while the reaction calculation module computes source or sink terms of charged and neutral species in the N_2/SF_6 plasma. The discharge and flow modules with different time scales in their movement are linked together by a time-slicing method.

From the results of the base simulation condition, the high electric field induced by the spray hole generates a large amount

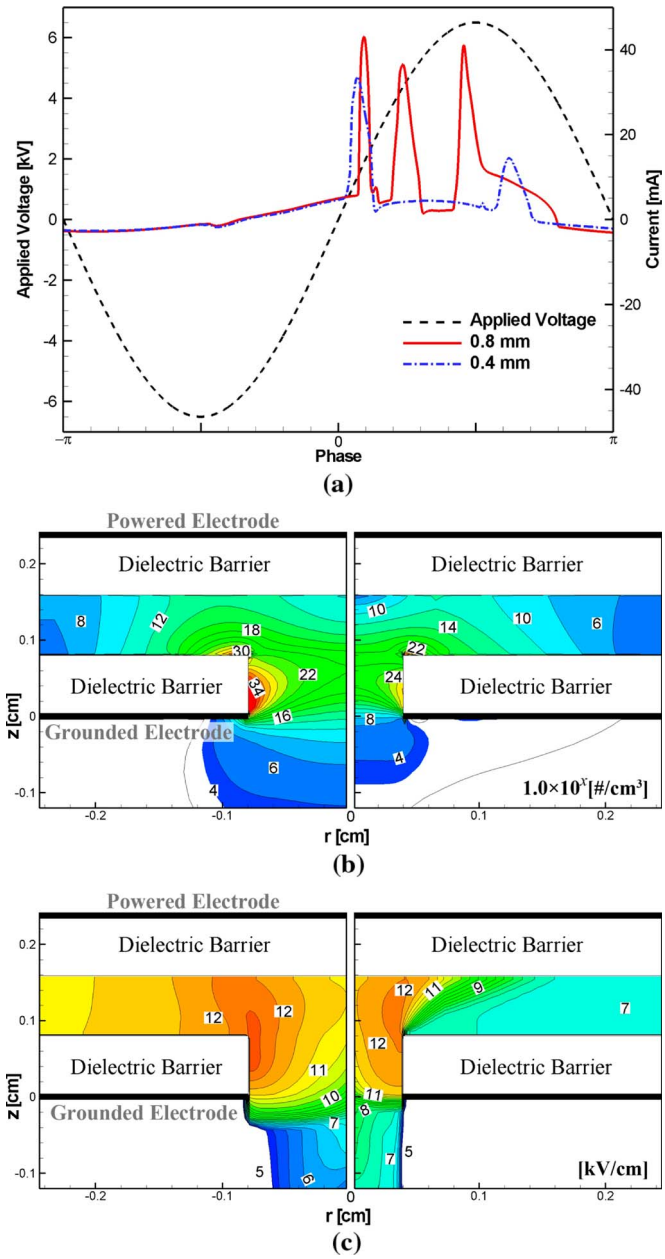

Fig. 7. Comparison of the discharge characteristics between 0.8 and 0.4 mm of the spray hole radius in the spray-type DBD reactor: (a) applied voltage and discharge current profiles; (b) electric field distributions at the initial moment of first current pulse; and (c) electron density distributions at the peak moment of first current pulse. [The number at each contour in (c) indicates the order x of electron density in 10^x cm^{-3} unit.]

of charged particles and forms the localized discharge similar to the surface discharge. This localized discharge moves toward the powered electrode surface and along the top surface of the grounded electrode barrier. The average electron density rises up to 10^{13} cm^{-3} in the discharge and spray hole regions, and then, the electric field decreases, and electrons are decayed to the generation of the next localized discharge. These repeated localized discharges yield a pulsed profile of discharge current during the positive period of the applied voltage. However, when a negative voltage is applied to the reactor, the group behavior of electrons occurs from the powered electrode barrier, but the electron density is too low to affect the discharge current

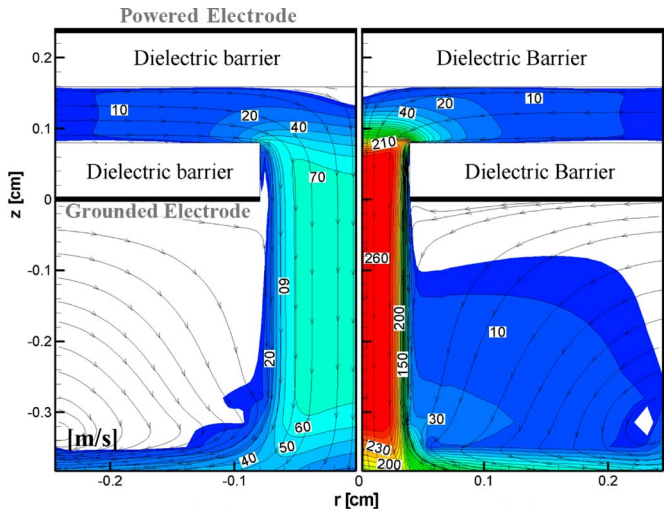

Fig. 8. Comparison of average advective velocity contours between (left) 0.8 mm and (right) 0.4 mm of the spray hole radius in the spray-type DBD reactor.

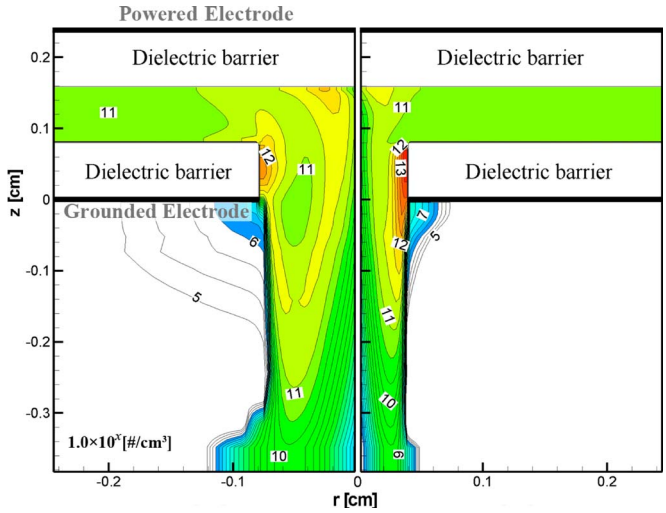

Fig. 9. Comparison of fluorine atom density distributions between (left) 0.8 mm and (right) 0.4 mm of the spray hole radius in the spray-type DBD reactor. (The number at each contour indicates the order x of density in 10^x cm^{-3} unit.)

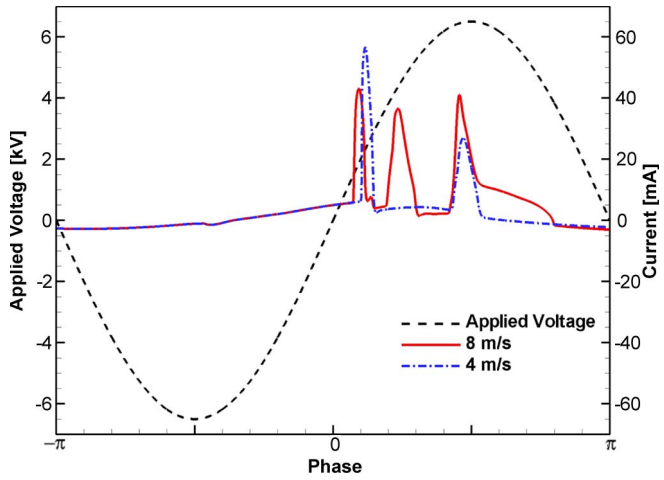

Fig. 10. Applied voltage and discharge current profiles for inlet flow velocities of 8 and 4 m/s in the spray-type DBD reactor.

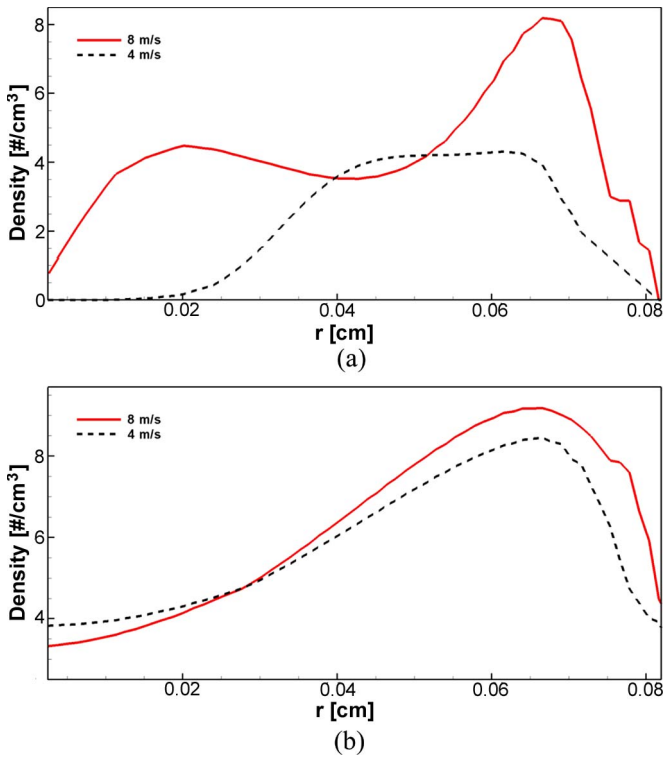

Fig. 11. Radial density distributions of (a) meta-stable species $N_2(a'^1\Sigma_u^-)$ and (b) the N_4^+ ion on the spray hole exit surface for inlet flow velocities of 8 and 4 m/s.

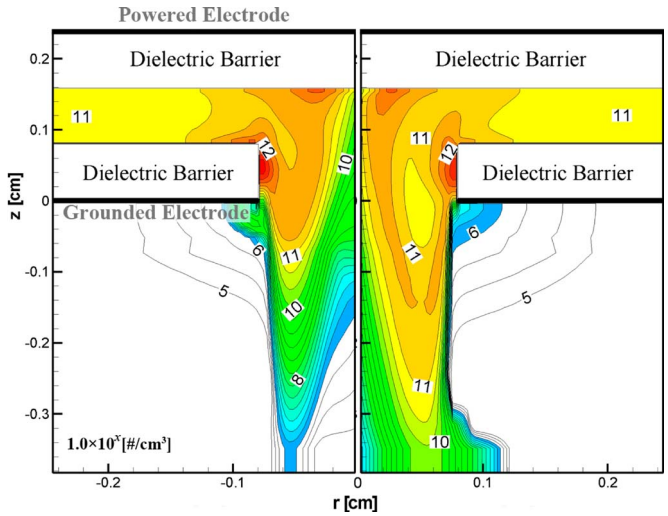

Fig. 12. Comparison of fluorine atom density distributions between (left) 4 m/s and (right) 8 m/s of the inlet flow velocity in the spray-type DBD reactor. (The number at each contour indicates the order x of density in 10^x cm^{-3} unit.)

to have a pulsed peak. The fluorine atoms are mainly produced by energetic electrons during the surface discharge along the spray hole barrier. A high fluorine density distribution is formed on the spray hole barrier wall and is maintained all the way through the spray region. Therefore, the spray hole geometry has an influence on the fluorine density distribution in the spray region.

From the numerical results obtained for the reduced spray hole radius, the discharge current profile has reduced intensity and number of peaks along with a longer interval between current peaks. This current profile is caused by a high-electron-density region shrunken by the lower electric field due to the smaller radius. Because of the narrower spray hole, the advective velocity in the spray hole region is much faster, so the effluent rate of fluorine atoms and the spatial difference in effluence are considerably increased in the spray region. These results indicate that the smaller spray hole reduces the influence on the discharge characteristics and has the advantage of processing rate enhancement in the spray region, but it is disadvantageous to the large-area uniform processing on the substrate.

The discharge current characteristics are changed by the lower inlet flow velocity to the reduced number of current peak and its widened interval. This phenomenon is analyzed by interactions between two meta-stables ($N_2(A^3\Sigma_u^+)$ and $N2(a'^1\Sigma_u^-)$) and the N_4^+ ion. The densities of the two meta-stables are reduced as the flow velocity decreases, and therefore, the production rate of N_4^+ ion is lowered. Then, the rising time of electric potential is extended by the slow increase of N_4^+ ion density at the spray hole exit. As a result, the variation of advective flow affects the discharge characteristics through interactions among meta-stables and ion. As inlet flow velocity is increased, the high-density areas of fluorine in the discharge and spray hole regions are increasingly narrowed since the residence time of the fluorine atom becomes shorter. However, the average density of the fluorine atom ejected into the spray region is increased by the faster transport of neutral particles.

REFERENCES

[1] U. Kogelschatz, "Dielectric-barrier discharges: Their history, discharge physics, and industrial applications," *Plasma Chem. Plasma Process.*, vol. 23, no. 1, pp. 1–46, Mar. 2003.

[2] B. M. Penetrante, M. C. Hsiao, J. N. Bardsley, B. T. Merritt, G. E. Vogtlin, A. Kuthi, C. P. Burkhart, and J. R. Bayless, "Identification of mechanisms for decomposition of air pollutants by non-thermal plasma processing," *Plasma Sources Sci. Technol.*, vol. 6, no. 3, pp. 251–259, Aug. 1997.

[3] L. A. Rosocha, "Nonthermal plasma applications to the environment: Gaseous electronics and power conditioning," *IEEE Trans. Plasma Sci.*, vol. 33, no. 1, pp. 129–137, Feb. 2005.

[4] N. Gherardi, S. Martin, and F. Massines, "New approach to SiO_2 deposit using a N_2-SiH_4-N_2O glow dielectric barrier-controlled discharge at atmospheric pressure," *J. Phys. D, Appl. Phys.*, vol. 33, no. 19, pp. L104–L108, Oct. 2000.

[5] A. Schütze, J. Y. Jeong, S. E. Babayan, J. Park, G. S. Selwyn, and R. F. Hicks, "The atmospheric-pressure plasma jet: A review and comparison to other plasma sources," *IEEE Trans. Plasma Sci.*, vol. 26, no. 6, pp. 1685–1694, Dec. 1998.

[6] H. Baránková and L. Bárdoš, "Hollow cathode atmospheric pressure plasma sources for surface treatment," *Surf. Coat. Technol.*, vol. 174/175, pp. 63–67, Sep./Oct. 2003.

[7] M. Štefečka, M. Kando, M. Černák, D. Korzec, E. G. Finantu-Dinu, G. L. Dinu, and J. Engemann, "Spatial distribution of surface treatment efficiency in coplanar barrier discharge operated with oxygen–nitrogen gas mixtures," *Surf. Coat. Technol.*, vol. 174/175, pp. 553–558, Sep./Oct. 2003.

[8] J. R. Roth, J. Rahel, X. Dai, and D. M. Sherman, "The physics and phenomenology of one atmosphere uniform glow discharge plasma (OAUGDP) reactors for surface treatment applications," *J. Phys. D, Appl. Phys.*, vol. 38, no. 4, pp. 555–567, Feb. 2005.

[9] G. E. Georghiou, A. P. Papadakis, R. Morrow, and A. C. Metaxas, "Numerical modelling of atmospheric pressure gas discharges leading to plasma production," *J. Phys. D, Appl. Phys.*, vol. 38, no. 20, pp. R303–R328, Oct. 2005.

[10] D. Lee, J. M. Park, S. H. Hong, and Y. Kim, "Numerical simulation on mode transition of atmospheric dielectric barrier discharge in helium–oxygen mixture," *IEEE Trans. Plasma Sci.*, vol. 33, no. 2, pp. 949–957, Apr. 2005.

[11] A. M. Howatson, *An Introduction to Gas Discharges*. New York: Pergamon, 1976.
[12] R. Morrow and N. Sato, "Discharge current induced by the motion of charged particles in time-dependent electric fields; Sato's equation extended," *J. Phys. D, Appl. Phys.*, vol. 32, no. 5, pp. L20–L22, Mar. 1999.
[13] W. S. Kang, J. M. Park, Y. Kim, and S. H. Hong, "Numerical study on influences of barrier arrangements on dielectric barrier discharge characteristics," *IEEE Trans. Plasma Sci.*, vol. 31, no. 4, pp. 504–510, Aug. 2003.
[14] J. H. Ferziger and M. Peric, *Computational Method for Fluid Dynamics*. Berlin, Germany: Springer-Verlag, 2002.
[15] B. V. Leer, "On numerical dispersion by upwind differencing," *Appl. Numer. Math.*, vol. 2, no. 3–5, pp. 379–384, Oct. 1986.
[16] T. A. Davies. [Online]. Available: http://www.cise.ufl.edu/research/sparse/umfpack
[17] M. J. Kushner, "Modelling of microdischarge devices: Plasma and gas dynamics," *J. Phys. D, Appl. Phys.*, vol. 38, no. 11, pp. 1633–1643, Jun. 2005.
[18] S. V. Patankar, *Numerical Heat Transfer and Fluid Flow*. New York: McGraw-Hill, 1980.
[19] KINEMA, *Software*. [Online]. Available: http://www.siglo-kinema.com
[20] G. J. Pietsch, "Peculiarities of dielectric barrier discharges," *Contrib. Plasma Phys.*, vol. 41, no. 6, pp. 620–628, Nov. 2001.
[21] H. E. Wagner, R. Brandenburg, K. V. Kozlov, A. Sonnenfeld, P. Michel, and J. F. Behnke, "The barrier discharge: Basic properties and applications to surface treatment," *Vacuum*, vol. 71, no. 3, pp. 417–436, May 2003.
[22] J. I. Kim, J. M. Park, D. Lee, S. I. Choi, and S. H. Hong, "Two-dimensional modeling of filamentary mode of dielectric barrier discharge in nitrogen at atmospheric pressure," in *Proc. 17th Int. Symp. Plasma Chem.*, Toronto, ON, Canada, Aug. 7–12, 2005.
[23] R. Morrow, "A survey of the electron and ion transport properties of SF_6," *IEEE Trans. Plasma Sci.*, vol. PS-14, no. 3, pp. 234–239, Jun. 1986.
[24] J. I. Kim, "Numerical study on filamentary and homogeneous discharge characteristics of dielectric barrier discharge in nitrogen at atmospheric pressure," M.S. thesis, Dept. Nucl. Eng., Seoul Nat. Univ., Seoul, Korea, 2006.
[25] Y. H. Choi, J. H. Kim, and Y. S. Hwang, "One-dimensional discharge simulation of nitrogen DBD atmospheric pressure plasma," *Thin Solid Films*, vol. 506/507, pp. 389–395, May 2006.
[26] A. V. Phelps and R. J. Van Brunt, "Electron-transport, ionization, attachment, and dissociation coefficients in SF_6 and its mixtures," *J. Appl. Phys.*, vol. 64, no. 9, pp. 4269–4277, Nov. 1988.
[27] G. Peach, "Ionization of neutral atoms with outer 2p and 3p electrons by electron and proton impact," *J. Phys. B, At. Mol. Phys.*, vol. 1, no. 6, pp. 1088–1108, Nov. 1968.
[28] P. S. Ganas, "Excitation cross sections for electron collisions with sulfur atoms," *J. Chem. Phys.*, vol. 92, no. 4, pp. 2374–2376, Feb. 1990.
[29] G. J. Cliteur, K. Suzuki, K. C. Paul, and T. Sakuta, "SF_6-N_2 circuit-breaker arc modelling around current zero—Part 1: Free-recovery simulation using a collisional-radiative plasma model," *J. Phys. D, Appl. Phys.*, vol. 32, no. 4, pp. 478–493, Feb. 1999.
[30] L. E. Kline, D. K. Davies, C. L. Chen, and P. J. Chantry, "Dielectric properties for SF_6 and SF_6 mixtures predicted from basic data," *J. Appl. Phys.*, vol. 50, no. 11, pp. 6789–6796, Nov. 1979.
[31] P. J. Chantry, *Applied Atomic Collision Physics*, vol. III. New York: Academic, 1983.
[32] M. Hayashi and T. Nimura, "Calculation of electron swarm parameters in fluorine," *J. Appl. Phys.*, vol. 54, no. 9, pp. 4879–4882, Sep. 1983.
[33] J. B. Belhaouari, J. J. Gonzalez, and A. Gleizes, "Simulation of a decaying SF_6 arc plasma: Hydrodynamic and kinetic coupling study," *J. Phys. D, Appl. Phys.*, vol. 31, no. 10, pp. 1219–1232, May 1998.
[34] W. L. Morgan and A. Szöke, "Kinetic processes in $Ar-Kr-F_2$ laser mixtures," *Phys. Rev. A, Gen. Phys.*, vol. 23, no. 3, pp. 1256–1265, Mar. 1981.
[35] R. J. Hall, "Dissociative attachment and vibrational excitation of F_2 by slow electrons," *J. Chem. Phys.*, vol. 68, no. 4, pp. 1803–1807, Feb. 1978.
[36] K. S. Baliyan and A. K. Bhatia, "Electron-impact collision strengths for neutral fluorine," *Phys. Rev. A, Gen. Phys.*, vol. 50, no. 4, pp. 2981–2988, Oct. 1994.

Hyun-Su Kim was born in Busan, Korea, in 1982. He received the B.S. and M.S. degrees in nuclear engineering in 2006 and 2008, respectively, from Seoul National University, Seoul, Korea, where he is currently working toward the Ph.D. degree in energy system engineering.

His research interests are focused on the atmospheric pressure barrier discharge and metal surface modification using atmospheric pressure nonequilibrium plasmas.

Woo Seok Kang received the B.S. and M.S. degrees in nuclear engineering in 2000 and 2002, respectively, from Seoul National University, Seoul, Korea, where he is currently working toward the Ph.D. degree in nuclear engineering.

From 2002 to 2004, he was with the Korea Institute of Science and Technology Evaluation and Planning, where he managed national nuclear R&D programs. In 2004, he joined the Samsung Corning Company, Ltd., Seoul, and was involved in the R&D projects for the next-generation liquid-crystal display technologies. His research interests include the diagnosis and simulation of atmospheric pressure plasmas for material processing.

Gon-Ho Kim received the B.S. and M.S. degrees in nuclear engineering from Hanyang University, Seoul, Korea, and the Ph.D. degree in engineering physics from the University of Wisconsin, Madison, in 1993.

From 1993 to 1995, he was a Postdoctoral Research Fellow with the Center for Plasma Aided Manufacturing, University of Wisconsin. From 1995 to 2003, he was an Assistant and Associate Professor with the Department of Applied Physics, Hanyang University. Since 2003, he has been a Professor with the Department of Nuclear Engineering, Seoul National University, Seoul. His research interests include plasma diagnostics using electrical probes, the application of time-transient sheath, the development of large-area plasma source, plasma–wall interactions, plasma generation in the human body, and plasma-assisted nanotube modification.

Sang Hee Hong (M'87) received the B.S. degree in applied physics from Seoul National University, Seoul, Korea, in 1974, and the M.S. and Ph.D. degrees in electrical engineering from Colorado State University, Fort Collins, in 1975 and 1978, respectively.

In 1979, he joined Seoul National University, where he is currently a Professor of nuclear engineering. He spent a year with the University of Sydney, Sydney, N.S.W., Australia, in 1989 as a Visiting Professor. His principal areas of research in the U.S. and Australia were the stability analysis of MHD flows and the theory of rotating plasmas and plasma centrifuges. His research interests in Korea included the numerical modeling of tokamak plasmas and industrial processing plasmas. Recently, his research work has included tokamak transport modeling and the development of thermal and nonequilibrium plasma sources along with their applications to material and environmental processing.